THE JOURNAL OF PHYSICAL CHEMISTRY C
A JOURNAL OF THE AMERICAN CHEMICAL SOCIETY

pubs.acs.org/JPCC

Article

B_4C Composites with a TiB_2-C Core–Shell Microstructure Produced by Self-Propagating High-Temperature Synthesis-Assisted Spark Plasma Sintering

Filiz Çınar Şahin,* Mubashir Mansoor, Meral Cengiz, Burcu Apak, Leyla Yanmaz, Katalin Balazsi, Zsolt Fogarassy, Bora Derin, Gültekin Göller, and Onuralp Yücel

Cite This: https://doi.org/10.1021/acs.jpcc.2c06179

Read Online

ACCESS | Metrics & More | Article Recommendations

ABSTRACT: Square-shaped boron carbide ceramic composites have been produced by spark plasma sintering with the addition of 5 to 20 vol % titanium metal powder in the B_4C matrix in order to initiate an in situ self-propagating high-temperature synthesis (SHS) of TiB_2. The SHS reaction not only enhances many of the physical and mechanical properties of B_4C, but also reduces the required sintering temperature and pressure because of the enthalpy of reaction between metallic Ti and B_4C. Sintering has been carried out in the SPS-temperature range of 1450 to 1550 °C with a uniaxial pressure of 40 MPa and a dwell time of 4 min under a 1 atm argon atmosphere. The effects of various amounts of Ti additions and sintering temperature on the phase composition, density, hardness, fracture toughness, and microstructure are examined. X-ray diffraction and transmission electron microscopy evaluations have shown that added Ti completely transforms into TiB_2, resulting in a core–shell microstructure with a carbon core, surrounded by a TiB_2 shell in the B_4C matrix. Moreover, by carrying out a control experiment where TiB_2 was added instead of Ti, and performing a molecular dynamics simulation of the B_4C-Ti interface, the significance of the in situ SHS process has been validated.

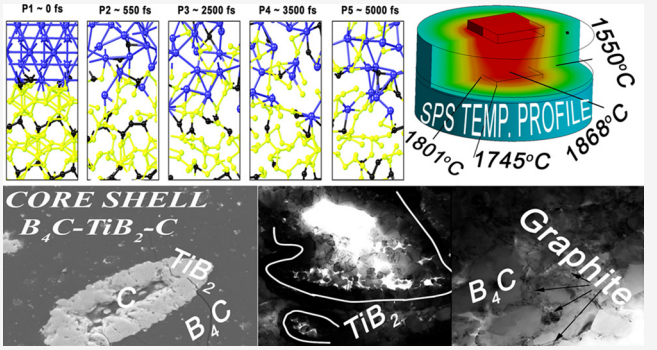

1. INTRODUCTION

Boron carbide (B_4C) exhibits excellent wear resistance, neutron absorption, resistance to chemical attacks, and superb hardness. It is known to be among the third hardest materials after diamond and cubic boron nitride at room temperature, while having a low density.[1] Because of their superior properties, B_4C ceramics are routinely used in many demanding areas, such as ballistic armors and nuclear reactors. However, sintering of B_4C ceramics poses significant challenges. The melting temperature of pure boron carbide is 2450 °C under 1 atmospheric pressure and therefore shows low self-diffusivity and low plasticity at most of the routinely used industrial-scale conventional sintering processes, as a result of its highly stable covalently bonded crystal structure.[2−5] Moreover, B_4C particles tend to contain a surface oxide layer identified as B_2O_3, which offers oxidation resistance in an ambient atmosphere, but on the other hand this oxide layer is difficult to remove completely even at elevated temperatures. The surface B_2O_3 layer creates secondary phases in the microstructure thus negatively impacting its tribological properties and makes the sintering of such ceramics challenging from this vantage point as well.[6] Therefore, B_4C ceramics with superior properties have only been possible to produce by high-temperature and high-pressure sintering techniques, under inert or reducing atmospheres.[5] Monolithic pure boron carbide ceramics have been reported with a relative density value of only up to 94.7% by pressureless sintering in a hydrogen atmosphere and extremely high temperatures of 2230 °C.[7] Aside from the difficulties in sintering of pure boron carbide, the most important mechanical weakness, even if sintered to high relative densities, is its low fracture toughness.[8] It is widely reported that the abovementioned two drawbacks of B_4C can be overcome by introducing an appropriately engineered second phase. An alternative approach is using nanoparticles to enhance the sinterability as a result of larger surface area of powder compact and enhanced mechanical properties of the material because of smaller grain sizes.

Received: August 29, 2022
Revised: November 9, 2022

Nevertheless, the issue of fracture toughness is most efficiently resolved by addition of appropriate second phases.[9−37]

Titanium diboride (TiB_2) has been identified as one of the most efficient sintering aids, which tends to reduce the sintering temperature and increases fracture toughness. The study done by Saeedi Heydari and Baharvandi[9] has very well documented the effects of TiB_2 addition on the hardness, fracture toughness, strength, and densification rates of B_4C ceramics. Although TiB_2 is directly added to B_4C in most studies,[12−17,21,32−34] some researchers have preferred to synthesize TiB_2 from TiO_2 and C starting powders during the sintering process.[17−19,26,31] The research by Skorokhod and Krstic[24] has shown that TiB_2 content obtained from the reaction of B_4C, TiO_2, and carbon black tends to reduce the activation energy for sintering of boron carbide ceramics in pressureless sintering of B_4C-TiB_2 composites, which also results in improved fracture toughness of up to 4.6 $MPa{\cdot}m^{1/2}$ for samples with 15 vol % TiB_2. The increase in the fracture toughness is correlated with increasing TiB_2 volume percentage, which leads to induced microcracking of the particle−matrix interface in the stress field of the approaching crack, thereby resulting in a resistance to formation of cracks because of the presence of local compressive stresses in the matrix.[24] The reduction in activation energy for sintering can be attributed to enthalpies of in situ reactions involved.

B4C-TiB2 composites have been produced by various different sintering techniques such as traditional pressureless sintering,[13−20] hot pressing,[21−27] hot isostatic pressing,[28] and spark plasma sintering (SPS).[30−37] Although each method has had its own advantages, SPS is a relatively new method that has proven to be exceptionally promising for sintering of B_4C composites when compared to traditional sintering methods. Among the advantages of SPS are its fast sintering time of only a few minutes and comparatively lower sintering temperatures that lead to lower energy consumption and its capacity for preventing grain coarsening which are of significant importance. In contrast to traditional sintering, which requires sintering durations of several hours that leads to excessive grain growth and deteriorated mechanical properties, the SPS method facilitates densification in a matter of minutes, thanks to the discharge between particles and thus limits the grain growth, which leads to enhanced mechanical properties. SPS is also capable of limiting the evaporation-condensation mechanism during a heating regime, which directly enhances the densification rate, as described in detail by Olevsky and Froyen.[38] Thus, ceramic composite materials produced through SPS have the potential for exhibiting better physical and mechanical properties.[39,40] All SPS systems to date are made of a uniaxial hydraulic press with an electrically conductive spacer and die. The most commonly used die material is graphite, and powder to be sintered is placed in between two punches such that once electric current passes through the system. If the powder is electrically conductive, it may be considered as a parallel ohmic load, and if an insulator, the mold is a series ohmic load in the system.[41] In other words, joule heating shall be considered as the primary source of heat for the bulk volume of the powder compact. Nevertheless, the use of pulsed DC current is believed to facilitate electric discharges at the points of powder contacts and grain boundaries, making any gaps in the compact act very similar to capacitors and hence fusing them into a monolithic solid at a faster rate when compared to conventional sintering methods.[42] However, this is a topic of debate, and there is evidence as for negligible influence of pulsing rates and sparks.[43] Furthermore, one must be very cautious when referring to sintering temperatures in SPS systems, given that it is not possible to measure the exact temperature of the powder compact at the time of sintering through direct measurements by a pyrometer or a thermocouple, especially at higher temperatures. Therefore, SPS-temperature should not be confused with the sintering temperature. SPS-temperature is measured either from outside the die or through a hole within die, but not directly from the sample. Temperature sensing is usually carried out either through a vertically drilled hole in the punch or through a horizontal drill in die body. In both cases, deviations from the actual sintering temperature by several hundred degrees will be inevitable as demonstrated by Zavaliangos et al.[44] It should also be noted that based on the electrical resistivity of the powder material, and the mold, there can be significant temperature variations within the die as well. This is especially significant for electrically insulating powder compacts where joule heating of the die is responsible for heating of the compact indirectly. Such temperature variations within the die can result in density variations when comparing different regions of a sintered ceramic.[40,45] In other words, temperature distributions in a die depend on the die geometry, physical properties of the material being sintered, and utilized electrical loading parameters at the time of experiments.

An emerging trend in SPS studies is the use of starting powders that go through exothermic reactions in order to yield the final desired composition.[46,47] The heat produced during exothermic reactions tends to cause a reduction in the sintering temperature, which facilitates easier densification. Generally, if the adiabatic temperature of an in situ exothermic reaction, which can be calculated based on the enthalpy of the reaction and heat capacities of the products, is less than 1200 °C, a combustion does not occur, but for adiabatic temperatures between 1200 and 2200 °C, a combustion synthesis does occur, while the reaction front cannot propagate. Meanwhile, for adiabatic temperatures above 2200 °C, a self-propagating high-temperature synthesis (SHS) is inevitable. A detailed description of the SHS reaction mechanism is given by Moore and Feng.[48] The ignition of such in situ SHS reactions within an SPS system may be influenced by a variety of factors, such as the preheat temperature or electric field intensity. The B-C-Ti ternary system is well documented in the literature,[49,50] and it is known that a reaction between B_4C and metallic Ti is highly exothermic and a candidate for an SHS reaction.[51] Therefore, in this study, we aimed to observe the impacts of adding Ti metallic powder on boron carbide ceramics and facilitate a process of SHS-assisted SPS of B_4C composites in a square shaped geometry of 50 × 50 × 5 mm size, without any prior plastic forming. The properties and microstructure of the sintered composites are analyzed with respect to sintering SPS-temperature and Ti content. Furthermore, we have modeled the temperature distribution in the die through finite analysis and conducted a density functional theory-based molecular dynamics (DFT-MD) study of the B_4C-Ti interface in order to elucidate the reaction mechanisms and explain the final microstructure. CALPHAD-based thermodynamic simulation has also been used in order to explain the achieved phases and microstructure.

https://doi.org/10.1021/acs.jpcc.2c06179
J. Phys. Chem. C XXXX, XXX, XXX−XXX

2. EXPERIMENTAL AND COMPUTATIONAL METHODS

2.1. Powder, Sintering, and Characterization Parameters. We have used HS grade B_4C and D grade TiB_2 powders from H.C. Starck Company, 99.8% pure Ti metal powders from Alfa Aeser, and Elftex 125 grade carbon produced by Cobot as the starting materials. The particle sizes and size distributions were measured by a Sedigraph Particle Size Analyzer. To measure the surface area of the ceramic and metallic powders, a Nova 2200e Surface Area & Pore Size Analyzer instrument was used, and the d_{50} and surface area values were recorded. The average particle size and surface areas of the powders used in the experiments are given in Table 1.

Table 1. Average Particle Size and BET Analysis for the Powders Used in Experiments

starting powders	d_{50} (μm)	surface area (m^2/g)
B_4C (HS Grade)	1.78	13.6
Ti (325 mesh)	26.46	0.38
TiB_2 (D-grade)	6.20	1.07
C (Elftex 125 grade)		27.01

Powder mixtures of 5, 10, 15, and 20 vol % Ti metal with the balance being B_4C were then prepared. The corresponding wt % values were weighed and mixed by ball milling with ethanol (Merck) using tungsten carbide balls for a total duration of 24 h. After sieving through a 100 μm screen, dried powders were directly loaded into a square shaped graphite mold, such that a sintered body of 50 × 50 × 5 mm dimensions could be produced. We have neither preshaped nor used any binder throughout the process.

SPS was carried out by SPS 7.40 MKVII, manufactured by SPS Syntex Inc. A current-controlled electrical supply of pulsed DC voltage has been used with a 12 ms on and 2 ms off pulsing sequence. The same pulsing frequency is applied for all experiments. A constant heating rate of 100 °C/min was used for all samples, with 4 min of dwell time at SPS-temperatures of 1450, 1500, and 1550 °C. The applied uni-axial pressure was kept constant at 40 MPa for all samples. The sintering atmosphere was 1 atm argon. The abovementioned sintering temperatures have been measured through an emissivity corrected single-wavelength optical pyrometer which has been focused onto a hole, drilled half-way between the sample and outer peripheries of the die as shown schematically in Section 3.2. The displacement of the lower spacer was also monitored and recorded throughout the experiments. These data were used to plot the displacement along with respect to time, so that shrinkage and sample expansion behavior can be monitored indirectly.

To investigate the outcomes in case TiB_2 was to be used as a sintering aid instead of Ti, a control experiment was performed using a powder mixture of 3.4 vol % carbon and 14.8 vol % TiB_2 with the balance being B_4C, which corresponds to the TiB_2 and Carbon content in 10 vol % Ti containing B_4C powder batch. The mixture was ball-milled and spark plasma sintered at a SPS-temperature of 1550 °C with all other parameters kept constant. The choice of this temperature is mainly due to its optimal outcomes in the SHS-assisted sintered samples (see Section 3.1).

The crystalline phases of powder mixtures after milling and densified samples obtained after SPS were examined by X-ray diffraction (XRD) (Geigerflex, Rigaku Corp). The sintered samples were sandblasted and divided into nine smaller square shaped sections using a diamond-coated blade, in order to characterize the center and corners separately. The relative density of each section was then measured, based on the Archimedes principle by using an AND-1653 model density determination kit. All the samples were polished using 1 μm diamond paste in order to achieve a flat, mirror-like surface. Hardness and fracture toughness of the samples were measured by the indentation method with Leica VH-MOT brand Vickers micro-hardness measurement apparatus with a dwell time of 12 s under a load of 9.8 N. Hardness and fracture toughness values were only measured from the central sections of samples which have reached 100% of theoretical density in order to make comparisons possible and to eliminate impacts of any residual porosity. The fracture toughness value of each sample was estimated using the Palmqvist indentation method by using eq 1, where Hv represents the Vickers hardness value, a is half the length of diagonal, E is the elastic modulus of the samples, and l represents the Palmqvist crack length.

$$Kc = 0.0264 \times \frac{Hv \cdot a}{\sqrt{l}} \left(\frac{E}{Hv}\right)^{0.4} \quad (1)$$

The microstructures of the samples were observed by using a scanning electron microscope (SEM; Model JSM 7000F, JEOL) followed by examinations under a transmission electron microscope (TEM; Philips CM-20) for further understanding of the observed microstructure.

2.2. Finite Element Analysis of Temperature Profiles in the Die. SPS-temperature is not the actual sintering temperature at the center of an SPS-die. This phenomenon is well known among SPS researchers;[44] however, it is worthwhile to note that the temperature is not recorded directly from the sample, instead, from a particular distance within the die. In fact, even if the temperature was recorded from the sample, given that the electric current density is not homogeneous in an SPS-die, as shown by Sakkaki et al.,[52] an inevitable temperature profile forms within the samples. Although this factor is negligible for metallic samples,[53] the effect becomes significantly large for dielectrics or materials with high electrical resistivity, especially as the sample sizes increase. Therefore, a thermoelectric modeling of the SPS-die is essential to estimate the temperature profiles within the sample. Graphite does show significant variations in its thermoelectric properties between manufacturers, and even over time due to changes in its microstructure. It is therefore imperative to measure electric and thermal properties of the graphite used for an accurate thermoelectric modeling through finite element analysis.

To create a thermo-electrical model of the SPS-die, the electrical resistivity of the used graphite die has been measured experimentally by appropriately machining two of the graphite punches. The graphite resistor was then placed in a vacuum chamber of 20 Pa pressure, with the two leads connected to a voltage controlled power supply where voltage and current were recorded while the surface temperature of the resistor was measured by a dual wavelength optical pyrometer (LumaSense Impace ISR6) for a temperature range of 800 to 2100 °C and room temperature. The resistivity values as a function of temperature have been extrapolated for temperatures outside

https://doi.org/10.1021/acs.jpcc.2c06179
J. Phys. Chem. C XXXX, XXX, XXX−XXX

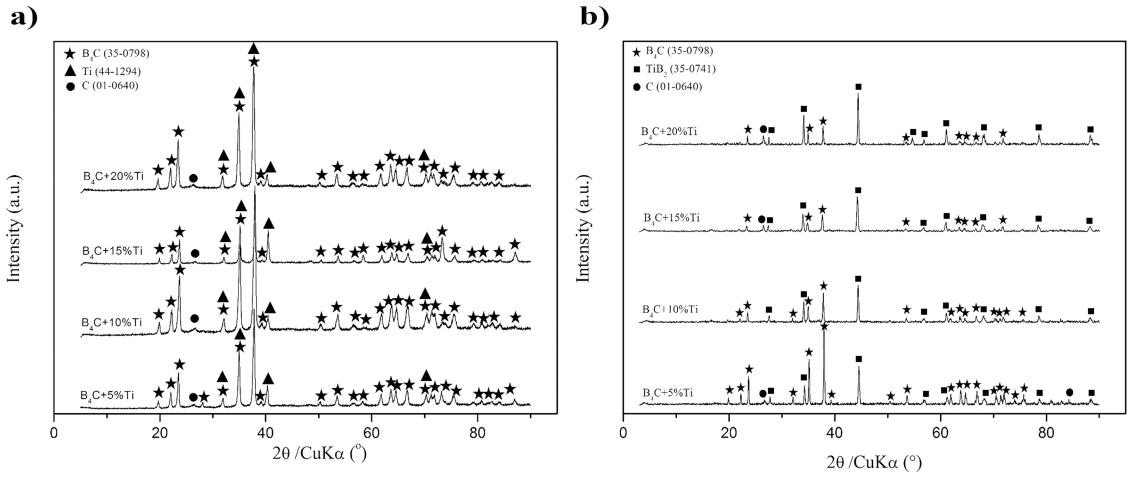

Figure 1. XRD data of the powder mixtures (a), and the final sintered composites (right) achieved after sintering at 1550 °C for a duration of 4 min. We observe a complete transformation of the Ti into TiB2 and an increase in C as well as a reduction of B4C content as the Ti percentage increases.

the measured range. Moreover, the thermal conductivity of the graphite die has been estimated by modeling of the resistor in order to match the experimentally recorded temperature profile and compared with the Wiedmann–Franz law[54] based on the resistivity values with respect to temperature. The thermal and electrical properties of TiB_2, C, and B_4C for the samples are retrieved from the literature.[55−58] A steady-state model of temperature distributions within the SPS-die was then created using the finite element analysis method through ANSYS software. The mathematical model used for thermoelectrical simulation is given as follows, and a similar methodology to the successful prior modeling studies.[52,55,56]

We have used the electric charge density equation for the determination of the electrical potential (U), as implemented by Nili et al.[56]

$$\nabla \cdot J = 0 \tag{2}$$

where J is the volumetric current density, which can be expressed as follows.

$$J = \rho E = -\rho \nabla U \tag{3}$$

Here, ρ is the electrical resistivity, which is a function of local temperature, and E is the electrical field intensity. Therefore, the electrical conduction can be expressed as in eq 4, where q_e is the heat generated due to electric current.

$$-\nabla \cdot (\rho \nabla U) = -\nabla q_e = 0 \tag{4}$$

It is then possible to apply to Fourier law of generation to calculate the local temperatures within the die, using eq 5.

$$\rho_d C_p \frac{\partial T}{\partial t} - \alpha \nabla^2 T = q_e + q_r \tag{5}$$

ρ_d is the local density, C_p is the heat capacity under constant pressure, and α is the heat conductivity. T is the temperature, and t represents time. The heat lost in a radiative manner is shown by q_r. The radiative loss can be expressed by the Stefan Boltzmann relation, as shown below, where P_v is the local power dissipated by an infinitesimal volume, v.

$$P_v = \sigma A_s \varepsilon (T_s^4 - T_c^4) \tag{6}$$

The A_s term is the surface area of v, and ε is the emissivity of component (taken as 0.8 for graphite). The T_s term is the surface temperature of the volumetric shape v, and T_c is the local temperature around the volume v. This term is often taken as the room temperature in a wide range of studies; however, because we have used a graphite felt enclosure around the die, a cavity effect is formed. Therefore, the temperature T_c will be the local temperature within the insulated enclosure. To calculate this temperature, we have used an iterative approach based on the Stefan Boltzmann law, as demonstrated in eq 7, where i represents the iteration number.

$$T_{c_{i+1}} = \sqrt[4]{\frac{P_v}{\sigma A_s \varepsilon} + T_{c_i}^4} \tag{7}$$

Therefore, the temperature of the outer surfaces of the die is set as the converged values of eq 7 with the convergence criteria being $T_{c_{i+1}} - T_{c_i} < 0.1$ K.

2.3. Thermochemical CALPHAD Model. Thermochemical modeling of the Ti-B_4C mixture was conducted by using FactSage 8.1 software[57] to estimate the possible products and adiabatic temperature values of the reactions between B_4C and Ti (eq 9). The SpMCBN database was used for the calculations of possible solid and liquid phases, whereas the FactPS database was selected for gas formations. In the calculations, the reactions were set as adiabatic ($\Delta H = 0$) at different initial temperatures.

2.4. Density Functional Theory-Based Molecular Dynamics. The B_4C-Ti interface is where the SHS reaction initiates and propagates. Therefore, in order to explain the final core–shell microstructure of the sintered samples (see Section 3.3), we have carried out a density functional theory-based molecular dynamics study of the interface (DFT-MD), where the forces and energies are fully computed through the generalized gradient approximation, as parametrized by Perdew–Burke–Ernzerhof (GGA-PBE exchange functional).[59] We have used the projector augmented wave method,[60] with a planewave cut-off energy of 300 eV. The Gaussian integration scheme is applied, with a smearing width of 0.05 eV. A time step of 4 fs is used for the dynamical simulation, and a total of 500 fs has been simulated. The NVE ensemble is used for the molecular dynamics calculations,[61] with the total energy and interface temperature recorded at every iteration. The benefit

https://doi.org/10.1021/acs.jpcc.2c06179
J. Phys. Chem. C XXXX, XXX, XXX−XXX

Table 2. Relative Densities of the Sintered Composites Based on the SPS-Temperatures and Added Ti Percentage[a]

Ti amount (vol %)	SPS-temperature (°C)	bulk relative density (%)	relative density of center (%)	relative density of corners (%)
5	1450	85.1 ± 0.3	88.4 ± 0.5	83.4 ± 0.3
	1500	88.9 ± 0.4	91.3 ± 0.6	85.2 ± 0.3
	1550	99.9 ± 0.1	100	99.5 ± 0.2
10	1450	86.2 ± 0.5	87.3 ± 0.5	82.6 ± 0.6
	1500	93.5 ± 0.2	97.1 ± 0.1	89.4 ± 0.5
	1550	99.0 ± 0.3	100	97.7 ± 0.3
15	1450	92.0 ± 0.5	94.2 ± 0.3	89.1 ± 0.8
	1500	100	99.8 ± 0.1	97.7 ± 0.3
	1550	100	100	100
20	1450	98.6 ± 0.3	100	94.6 ± 0.5
	1500	100	100	100
control exp.	1550	96.10 ± 0.5	98.3 ± 0.1	94.8 ± 0.2

[a]The densities are measured at the center and corners of the ceramics. The control experiment corresponds to the 10 vol % Ti; however, TiB_2 was used instead, as explained in Section 2.1.

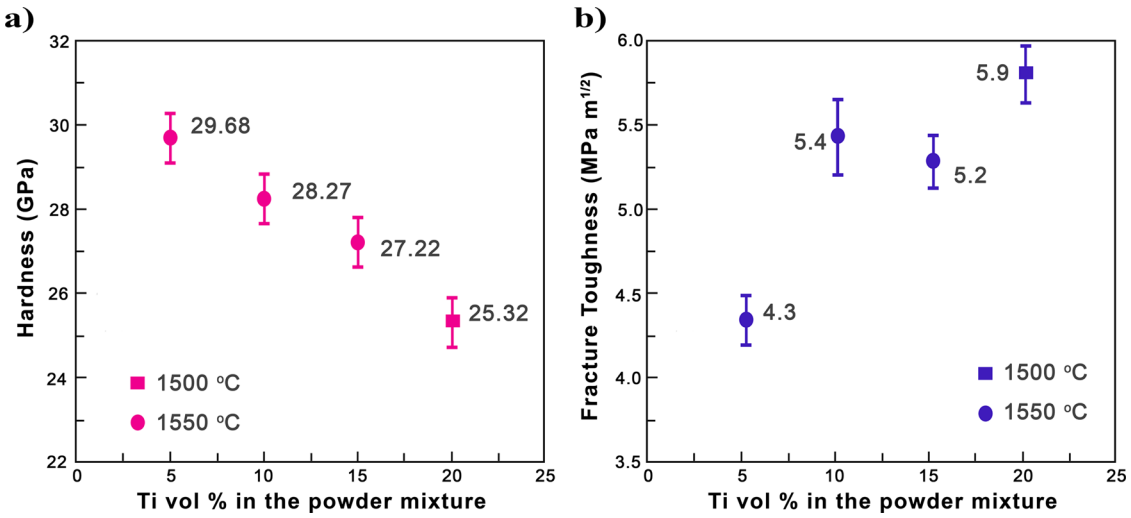

Figure 2. Hardness of the sintered composites decreases with increasing Ti percentage (a), while there is an increase in the fracture toughness with increasing Ti content (b). The hardness and fracture toughness values are obtained from fully dense samples.

of the NVE ensemble is the fully adiabatic nature of the simulation, where the total energy is supposed to remain constant in the absence of any exothermic or endothermic reactions. Therefore, the NVE ensemble makes it possible to investigate the supposedly SHS reactions at the interface, and the adiabatic temperature that should be expected, as previously demonstrated by Baras et al.[62] We have used the Vienna ab initio simulation package (VASP 6.1),[63] under the framework of the MedeA 3.4[64] for the DFT-MD simulation of the interface. The pair correlation functions, $g(r)$, in the initial and final conditions have been compared, as calculated by eq 8.[65]

$$g(r) = \frac{dn_r}{4\pi r^2 \rho dr} \tag{8}$$

The calculated $g(r)$ functions are used for investigating any phase transformations from solid to liquid at the interface.

3. RESULTS AND DISCUSSION

3.1. Bulk Properties of the Sintered Composites. The XRD patterns of the prepared powder mixture before and after sintering are shown in Figure 1. There are no metallic Ti peaks in any of the sintered samples, and we observe a complete transformation of the Ti into TiB_2. Moreover, the composites with a greater Ti content in the starting powder mixture exhibit a higher TiB_2 percentage and a lower B_4C peak intensity. There is also an increase in the intensity of free carbon peaks after sintering, with increasing Ti percentage in the mixture, making it clear that Ti and B_4C have gone through the following reaction.

$$B_4C + 2Ti \rightarrow 2TiB_2 + C \tag{9}$$

The reactions between B_4C and Ti are widely reported in the literature[66−69] and known to be highly exothermic. The nature of this reaction between titanium metal and boron carbide powders can be classified as a SHS, given that it has an adiabatic temperature of more than 2200 °C.[69] Although the majority of studies report TiC formation, the B_4C/Ti ratio used in this study inhibits the formation of any TiC phase.

The relative density values of all sintered samples are tabulated in Table 2. Increasing Ti content results in a drastic increase of the relative densities and fracture toughness values while the hardness has a decreasing trend as shown in Figure 2, which is also consistent with the findings of Liu et al.[70] on B_4C-TiB_2 ceramics. Similarly, the increase in fracture toughness with increasing Ti is associated with the inherently higher fracture toughness of the TiB_2 and C (graphite) phases that increase in proportion as well.

https://doi.org/10.1021/acs.jpcc.2c06179
J. Phys. Chem. C XXXX, XXX, XXX−XXX

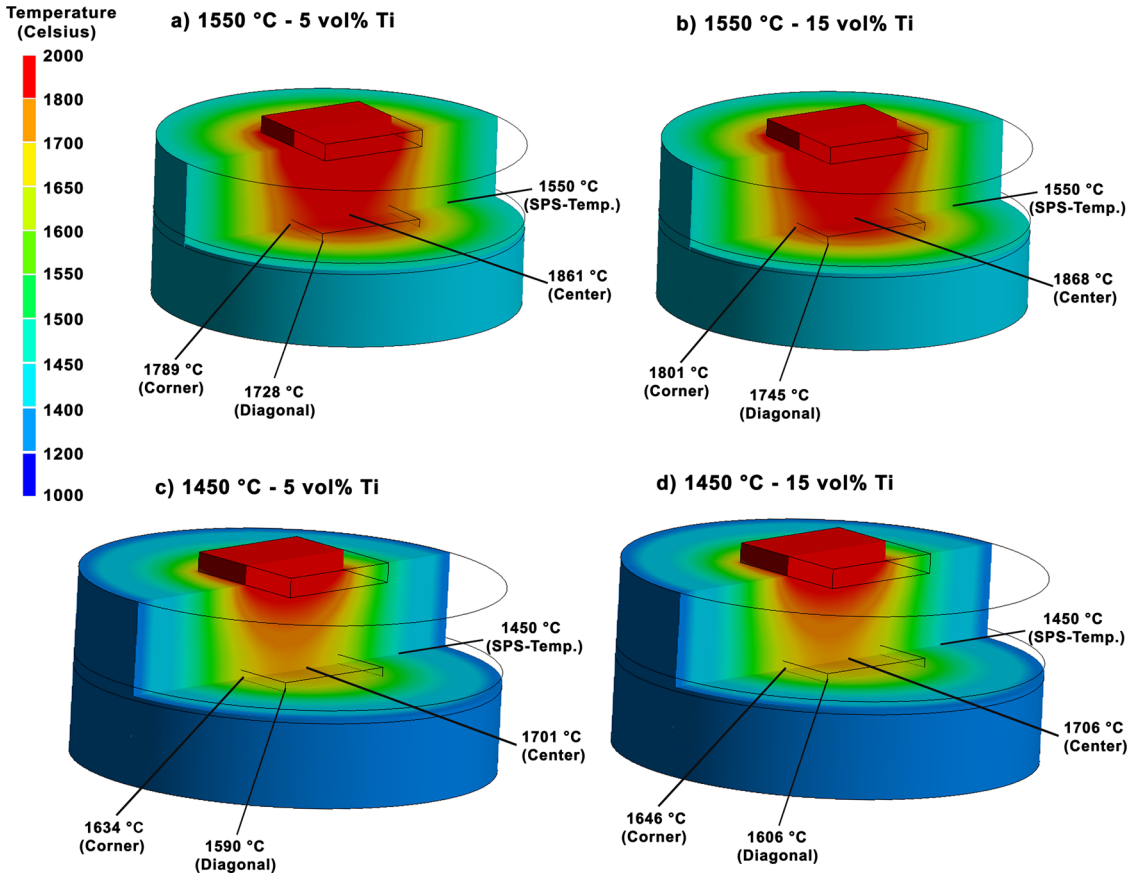

Figure 3. Thermoelectric simulation of the SPS die based on the sample composition and SPS-temperature is demonstrated. A significant temperature difference exists within the die, which affects the relative density of the sintered samples measured from the center, or corners.

3.2. Relative Density and Temperature Variations across the SPS-Die. The relative density of the central section of all samples sintered at a SPS-temperature of 1550 °C has reached 100% of the theoretical density. However, we also observe a difference between the relative density values obtained from the center of samples in comparison to the corners (Table 2). This variation in density is a result of temperature variations within the die, which is found to be highest in the center and lowest in the corners and farthest diagonals, as calculated by the steady-state thermoelectric simulation of the die, shown in Figure 3.

Increasing SPS-temperature shows a reduction in the difference of relative densities between the center and corners of samples, rendering the SPS-temperature as an important factor in homogenization of sintered composite's properties. Our calculations demonstrate that the temperature at the center of die, in the absence of any in situ SHS reactions, is approximately 250 to 300 °C higher than the measured SPS-temperature. We also note that there is a difference of approximately 100 to 150 °C between the center and the farthest diagonals of the die. It is noteworthy that these values are strongly dependent on the properties of graphite and the dimensions of the die used. Nevertheless, regardless of the graphite properties, it is clear that such die geometry will always show a considerable temperature variation when comparing the corners to center, especially for electrically insulating samples. These results are consistent with prior computational models by Zavaliangos et al.[44] and Olevsky et al.,[71] who have demonstrated similar temperature variations between the center of the SPS-die and the outer peripheries.

3.3. Microstructure of the Sintered Composites. SEM micrographs from 5, 10, 15, and 20 vol % Ti containing samples are shown in Figure 4. We observed the presence of a core−shell region within the matrix, where the grains are not of the same chemical composition entirely (Figure 5). Energy-dispersive spectroscopy results from several points have shown a significantly higher concentration of Ti in the outer peripheries of this nodular structure, and an increase in the carbon, and reduction in Ti contents as we approach the center of this structure. The conclusive analysis of the phases was achieved through TEM analysis, where the presence of an outer TiB_2 shell within the B_4C matrix is observed, and a carbon phase concentrated in the center. The same microstructure is observed in all samples, regardless of the sintering temperatures or Ti percentage. In other words, all samples show a core−shell microstructure with a TiB_2 shell and a sub-micron carbon phase within the core inside the B_4C matrix. It is noteworthy that the approximate diameter of the TiB_2 shell corresponds to the average particle size of the metallic Ti powder used. Further analysis by TEM on 20% Ti containing samples has confirmed the presence of an amorphous carbon and graphite phase with a sub-micron grain size in the central core, as shown by the electron diffraction and TEM micrograph presented in Figure 6.

The benefit of this core−shell microstructure is the soft carbon core that positively affects the fracture toughness values, as prior studies on TiB_2 containing B_4C composites exhibit significantly lower values in this regard.[70] The formation of this microstructure is a direct consequence of the in situ SHS reaction, which has not only reduced the

https://doi.org/10.1021/acs.jpcc.2c06179
J. Phys. Chem. C XXXX, XXX, XXX−XXX

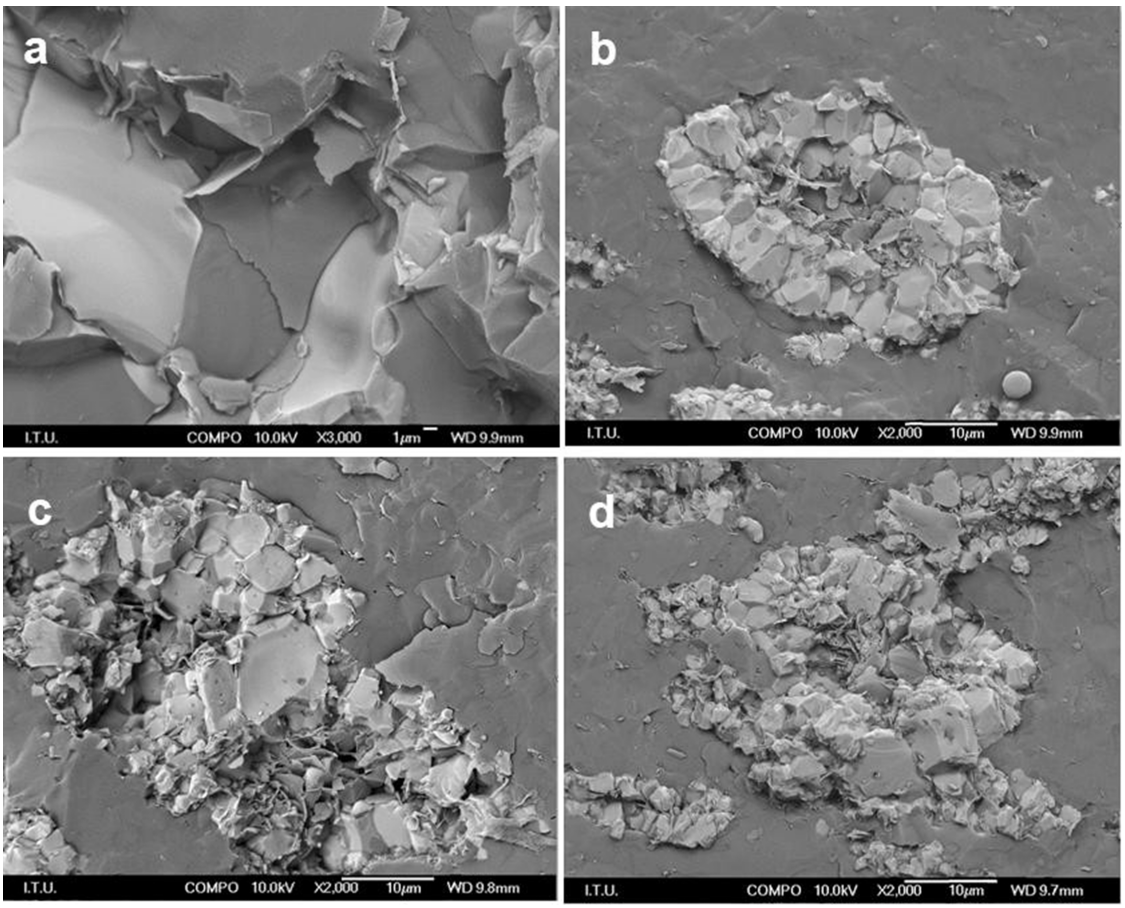

Figure 4. SEM micrographs from the fractured surfaces of the 5 vol % (a), 10 vol % (b), 15 vol % (c), and 20 vol % Ti (d) containing B_4C composites.

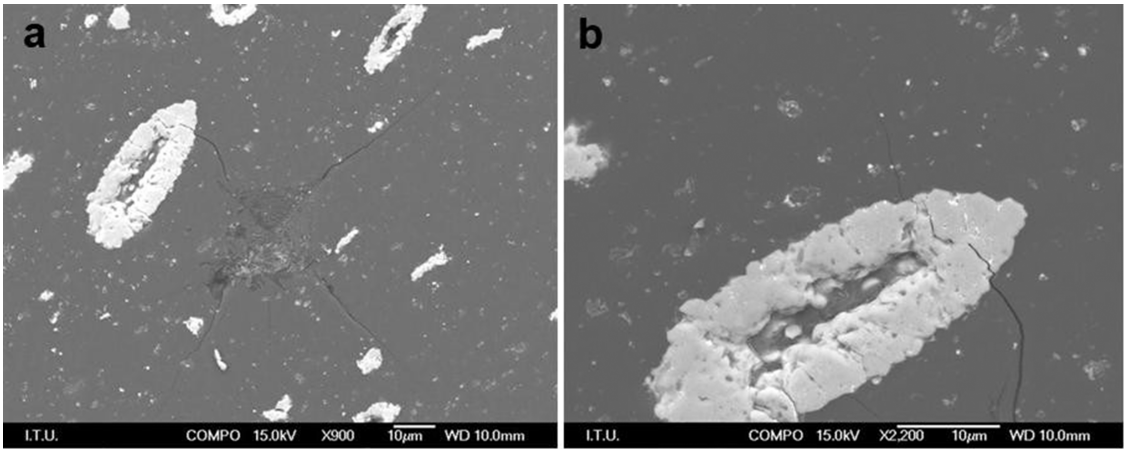

Figure 5. Backscattered SEM micrographs from the induced-crack propagation on 5 vol % Ti containing composites. The lighter shell-shaped regions are found to be TiB_2, surrounding an interior carbon core, demonstrating a core−shell microstructure.

required sintering temperature, but also enhanced the mechanical properties of the material, with the core−shell microstructure acting as crack deflection sites. We anticipate that the soft carbon core acts as crack-energy absorption sites and thus increases the fracture toughness values, which may also be explained through the rule of mixtures. Samples from the control experiment do not exhibit any form of a core−shell microstructure, which is consistent with a prior study of Liu et al.[70] where the starting powders were B_4C and TiB_2.

3.4. Impacts of the SHS Reaction and the Microstructural Evolution during Sintering. Analyzing the spacer displacement curves during sintering can provide valuable insight as reported numerous times, including the possibility to monitor occurrence of a chemical reaction.[72,73] The research by Nikzad et al.[35] is of particular interest given that they have successfully used the displacement data in order to differentiate between SHS and solid state reactions. Therefore, the displacement data of Ti-containing and the control experiment where TiB_2 was added have been compared

https://doi.org/10.1021/acs.jpcc.2c06179
J. Phys. Chem. C XXXX, XXX, XXX−XXX

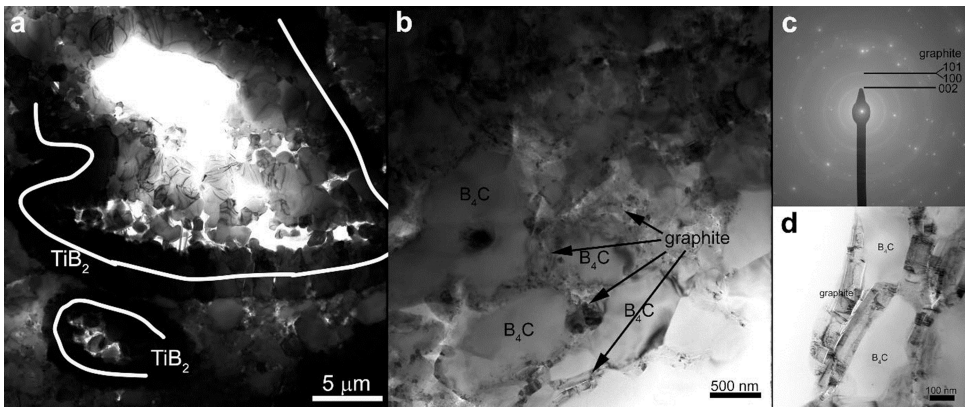

Figure 6. Bright-field TEM micrographs from the 20 vol % Ti containing composites are shown (a, b, and d), which demonstrate the core−shell structure. The electron diffraction from the center of the core−shell structure (c) exhibits a graphite structure, with a sub-micron size range.

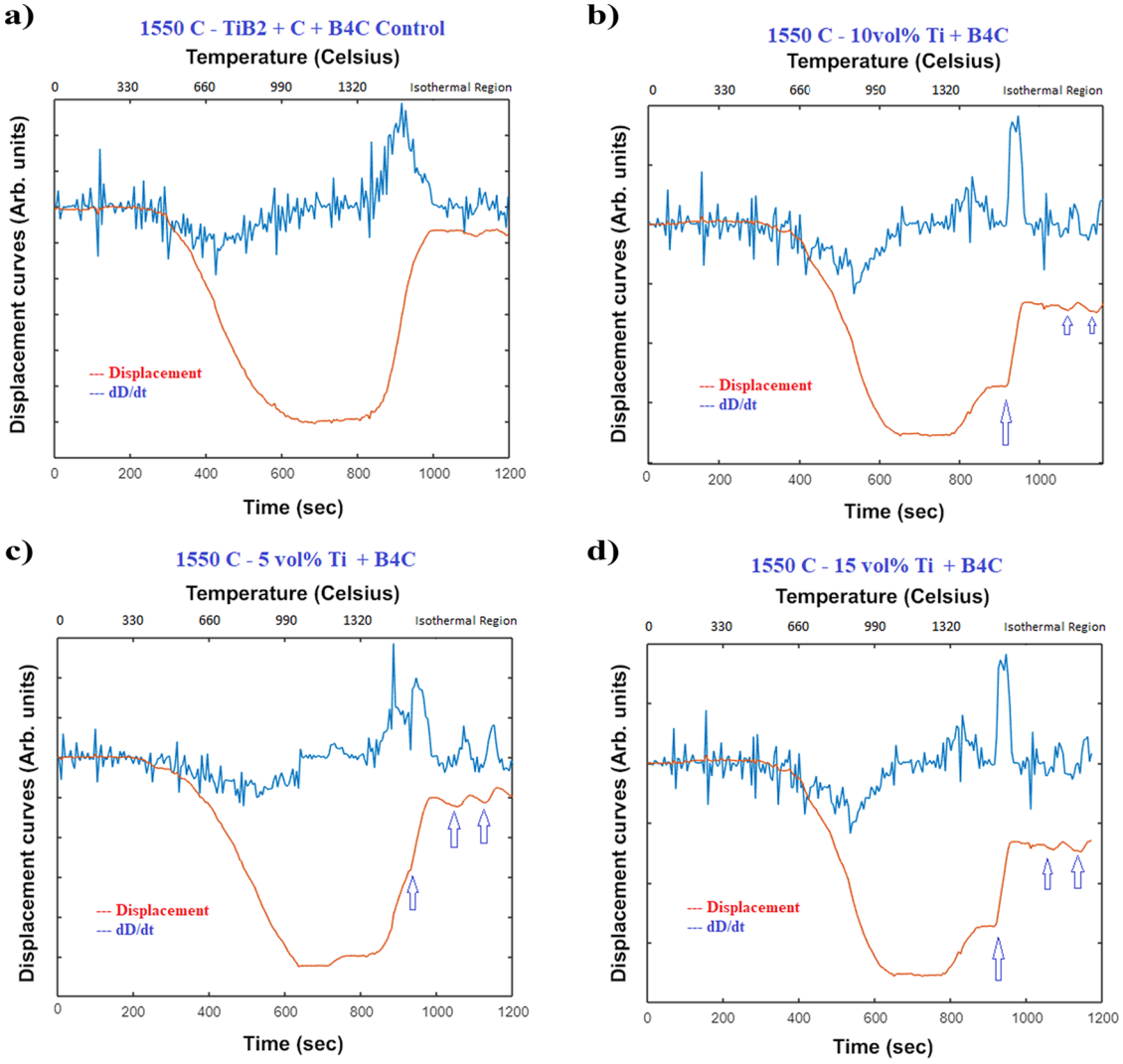

Figure 7. Displacement curves for the Ti containing powder mixtures exhibit a sharp increase in the shrinkage rate, at the onset of the isothermal region, which becomes steeper as the percent Ti increases. The blue curves show the rate of change in displacement with respect to time, and the arrows indicate regions where the rate of change in displacement shows a sharp rise that is attributed to the in situ SHS reaction.

and shown in Figure 7. It is clear that increasing Ti content tends to create a sharp increase in the rate of displacement with respect to time followed by subsequent fluctuations (shown by arrows in Figure 7b−d). The steep rise in displacement is recorded at a SPS-temperature of approximately 1500 °C, which should coincide with the temperature at which ignition for all Ti particles becomes inevitable. Such behavior is a strong evidence of an in situ SHS reaction, as demonstrated by Nikzad et al.[35] An additional noteworthy contrast between the control experiment with added TiB_2 and

https://doi.org/10.1021/acs.jpcc.2c06179
J. Phys. Chem. C XXXX, XXX, XXX−XXX

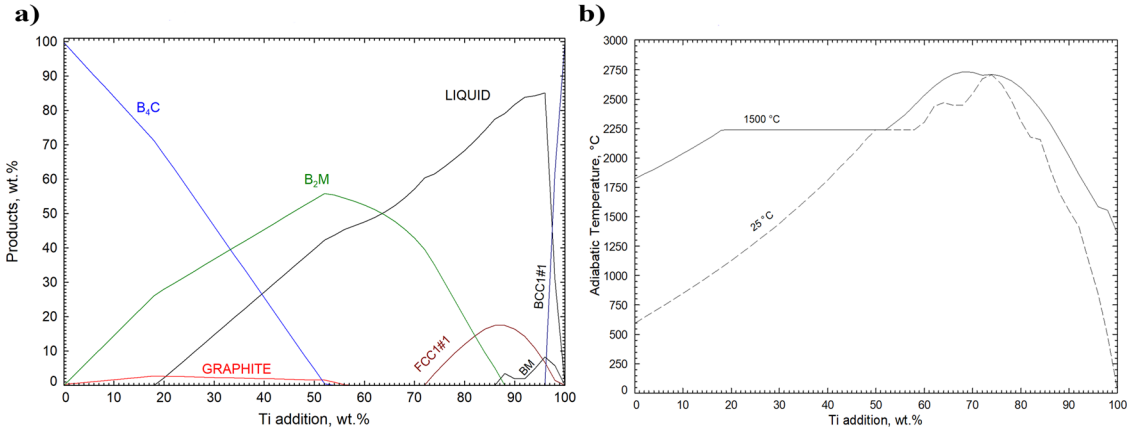

Figure 8. FactSage calculation for the effect of Ti addition to B4C at a preheating temperature of 1500 °C on products (a), FactSage calculation for the effect of Ti addition to B4C on adiabatic temperature values at different initial temperatures (i.e., 25 and 1500 °C) (b).

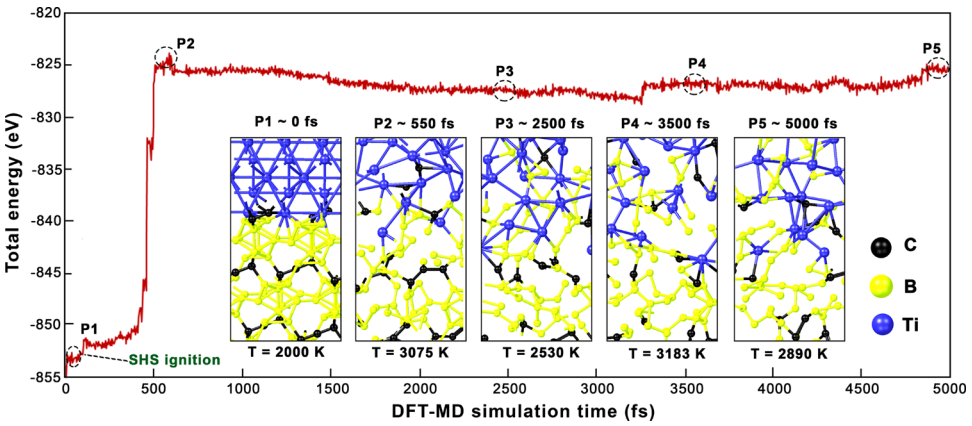

Figure 9. DFT-MD simulation conducted on the Ti metal and B_4C interface through NVE ensemble shows a rise in the total energy of the system, which is indicative of an exothermic process. A steep rise in temperature is observed at the onset of the simulation, attributed to the SHS-ignition, and the initial temperature of 2000 K is seen to rise to values above the melting point of the ternary Ti-B-C system that is also associated with an increase in interatomic spacings.

reactive-SPS with samples containing Ti is the net displacement recorded when comparing the isothermal regime with the initial start time of $t = 0$.

At first sight, it might be incorrectly interpreted that samples containing TiB_2 as a sintering aid have shown greater shrinkage; however, it is crucial to note that the displacement value is an aggregate of the die and sample expansion and its shrinkage factors combined,[73] as shown in eq 10, where D is the net displacement, and S is the total shrinkage. However, the total displacement depends on the thermal expansion of the sample, which is a function of temperature, represented by $E(T)$. The $E(T)$ term is negative because of the outward direction that we take as the negative direction.

$$D = S - E(T) \tag{10}$$

Therefore, if the sample is at a higher temperature due to the heat of reaction, the impact of expansion will be inevitably higher, hence, pushing the punches in the negative direction (outward), which will result in a greater distance from the initial baseline where the experiment started ($t = 0$). At the initial stages, the negative displacement is primarily associated with the expansion, which is the dominant factor, and at higher temperatures once the sample shrinkage imposes a greater contributing factor, a positive rate of change of displacement is seen. From this perspective, it is possible to say that powder mixtures containing a higher Ti content have been sintered at relatively higher temperatures throughout the SPS dwell time. When compared to the sample with the added TiB_2, the relatively lower gradient of the displacement curve at the onset of the iso-thermal region and the smaller net displacement D are both indicators of lower local sintering temperatures. We also observe a sharper rise in D as the total Ti percentage increases. In other words, this phenomena is due to the heat of reaction caused by the SHS reaction. It is not clear to us what the exact cause of ignition for such in situ SHS-assisted SPS is, and this question requires further investigation. The ignition of the SHS reaction may occur due to the sparks generated by the SPS system, the increase in the local temperature, and/or the electric field.

By considering the powder mixture at the atomistic level, it should be noted that the titanium metal particles become sites of local heat sources for the entire ceramic composite during the SHS reaction, which are ignited either through sparks of the pulsed DC current of SPS, or as a result of the increasing die temperature. The reaction can promote the sintering process by not just heating the mixture locally but also by creating a liquid phase reaction-front which tends to aggressively propagate toward the interior of the titanium particle until it is completely consumed, as evident by the thermo-chemical simulation shown in Figure 8. It should be

https://doi.org/10.1021/acs.jpcc.2c06179
J. Phys. Chem. C XXXX, XXX, XXX−XXX

noted that the local composition at a Ti particle site which goes through this reaction, regardless of the total mixture composition, is 66.6 mol % Ti and 33.3 mol % B_4C (due to the required stoichiometry at the SHS reaction front), resulting in an ultrahigh adiabatic temperature at the interface of the Ti metal and B_4C powders (Figure 8b). Therefore, the local temperature can reach approximately 2800 °C, as predicted by our thermochemical simulations. This extreme temperature at the interface is also seen in our DFT-MD simulation. As shown in Figure 9, we observe a steep rise in the total energy of the system, despite the NVE ensemble being fully adiabatic in nature, and thus this observed increase is associated with the onset of the SHS reaction due to breaking and formation of new bonds at the interface. The temperature which corresponds to the final stage is well beyond the melting point of the ternary mixture. By considering the ternary phase diagram of B-Ti-C,[74] it is clear that as a result of the SHS reaction that goes to completion within a few seconds,[75] the local temperature exceeds the liquidus temperature of the local composition and therefore, even if for a very short interval, a ternary liquid phase region is formed. The ternary liquid is not long lived enough for any capillary forces to propel the liquid within the bulk of the composite because of the immediate solidification due to heat transfer toward the surroundings and reduction in the local temperature as soon as the SHS reaction goes to completion. The appearance of this ternary liquid phase is proved by the pair correlation function $g(r)$, calculated through the molecular dynamics (Figure 10), which shows the

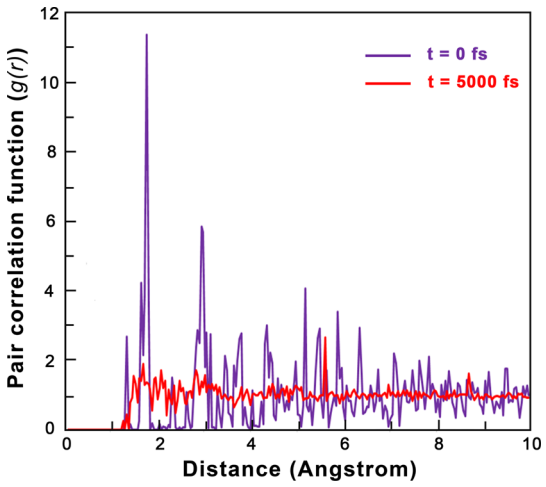

Figure 10. Pair correlation function for t = 0 fs (purple) shows the initial radial distribution of atoms at the beginning of the DFT-MD simulation. At t = 5000 fs (red), the distribution becomes more homogeneous and a loss of periodicity is seen, which are both indicative of the liquid state.

change in the spacing between atoms at the end of the simulation no longer correspond to a solid-state interface, but rather it is a characteristic of a liquid phase.

The formation of the core−shell microstructure is made possible through the solidification of this ternary liquid that should begin at the peripheries of the former Ti−B_4C interface and proceed toward the interior of the formerly present Ti particle's space, through heterogeneous nucleation on the surrounding B_4C grains. Based on the Ti-B-C ternary phase diagram, the solidification sequence for the composition used is B_4C, followed by TiB_2, and eventually ending in carbon growth, resulting in a core−shell microstructure, as seen in SEM and TEM micrographs. In other words, the formed core−shell microstructure, which shows concentration of carbon at the central core coupled with the fact that the diameter of the TiB_2 shell corresponds to the metallic Ti powder used, strongly suggests an in situ nucleation and growth from the liquid phase. This hypothesis is supported by the thermo-chemical and molecular dynamics simulations conducted in this study, as well as the thermodynamic solidification sequence that should be expected from a ternary liquid based on the Ti-B-C phase diagram.[74] Because of the heat of reaction at the SHS reaction front, the interface goes through a local melting, and formation of a ternary liquid phase is inevitable. As the heat is lost to the surrounding environment, as the sintering temperature is more than 1000 °C lower than the temperature at the reaction front, the ternary melt goes through a rapid crystal growth following the thermodynamic solidification sequence, causing a core shell microstructure. This process not only enhances the sintering, but also causes an increased fracture toughness, due to the unique microstructure that emerges.

4. CONCLUSIONS

We have demonstrated that an in situ SHS-SPS of B_4C composites can significantly enhance densification and lower the required sintering temperature. Our key findings on the metallic Ti containing B_4C powder mixture are as follows.

- SPS-temperature of 1550 °C, pressure of 40 MPa, and a sintering time of 4 min are sufficient for achieving the theoretical density in TiB_2 containing B_4C composite ceramics, when using 15 vol % Ti and B_4C as the starting powder mixture.
- The metallic Ti completely transforms into TiB_2, through an SHS reaction with B_4C. The adiabatic temperature at the reaction front is approximately 2800 °C, which causes melting of the interfaces, followed by crystal growth which follows the thermodynamic solidification path.
- Based on the composition used, we achieved a TiB_2 shell, with a C core within the B_4C matrix. This core−shell microstructure results in a relatively soft core and thus significantly improves the fracture toughness of the composites.
- Highest hardness values of 29.68 GPa were obtained in 5 vol % Ti containing B_4C composites, and the highest fracture toughness is measured in the 20 vol % Ti containing sample as 5.9 MPa·$m^{1/2}$. We observe an inverse correlation between hardness and fracture toughness in this ceramic system.
- Square shaped sample die geometry is inevitably subjected to a significantly lower temperature at the corners, due to the usually used die designs in the SPS systems, which causes a lower densification at the corners. However, increasing Ti content to 15% homogenizes the density across the samples and yields full theoretical density upon sintering at a SPS-temperature of 1500 °C.

4.1. Future Perspective. The promising results of the SHS-assisted SPS technique underscore the interesting possibilities for manufacturing ceramics which are otherwise difficult to sinter, and thus SHS-SPS requires further research in other ceramic systems. Moreover, the impact of DC pulsed

https://doi.org/10.1021/acs.jpcc.2c06179
J. Phys. Chem. C XXXX, XXX, XXX−XXX

current frequency on the ignition of the SHS reaction should be further studied. Research in this regard can shed light on the nature of ignitions and its impact on the displacement curves. A better understanding in this regard will influence the starting powder sizes and the choice of sintering parameters.

It is also clear that the temperature differences in a square-shaped geometry will become even more severe for larger sample sizes. This is a problem that should be dealt with in order to facilitate large-scale industrial use of SPS systems, and further research is required on how to create homogeneous die temperatures for larger electrically insulating samples, where joule heating is the primary source of heat for the bulk volume of sintered products. Novel die geometries are required in this regard, because currently used geometries cannot offer homogeneous temperatures.

AUTHOR INFORMATION

Corresponding Author

Filiz Çınar Şahin − *Metallurgical and Materials Engineering Department, Istanbul Technical University, Istanbul 34469, Turkey;* orcid.org/0000-0003-4465-3751; Phone: +902122857166; Email: cinar@itu.edu.tr; Fax: +902122853381

Authors

Mubashir Mansoor − *Metallurgical and Materials Engineering Department and Department of Applied Physics, Istanbul Technical University, Istanbul 34469, Turkey;* orcid.org/0000-0001-8097-8823

Meral Cengiz − *Metallurgical and Materials Engineering Department, Istanbul Technical University, Istanbul 34469, Turkey;* orcid.org/0000-0002-4596-8387

Burcu Apak − *Metallurgical and Materials Engineering Department, Istanbul Technical University, Istanbul 34469, Turkey*

Leyla Yanmaz − *Metallurgical and Materials Engineering Department, Istanbul Technical University, Istanbul 34469, Turkey;* orcid.org/0000-0001-6685-1412

Katalin Balazsi − *Centre for Energy Research, Institute of Technical Physics and Materials Science, Hungarian Academy of Sciences, Budapest 1051, Hungary*

Zsolt Fogarassy − *Centre for Energy Research, Institute of Technical Physics and Materials Science, Hungarian Academy of Sciences, Budapest 1051, Hungary*

Bora Derin − *Metallurgical and Materials Engineering Department, Istanbul Technical University, Istanbul 34469, Turkey*

Gültekin Göller − *Metallurgical and Materials Engineering Department, Istanbul Technical University, Istanbul 34469, Turkey*

Onuralp Yücel − *Metallurgical and Materials Engineering Department, Istanbul Technical University, Istanbul 34469, Turkey*

Complete contact information is available at: https://pubs.acs.org/10.1021/acs.jpcc.2c06179

Notes

The authors declare no competing financial interest.

ACKNOWLEDGMENTS

We appreciate the tremendous assistance of Hüseyin Sezer during the characterization stages. This study was partially supported by TUBITAK in the context of project number 213M163 and Scientific Research Project Funds of Istanbul Technical University under project number 370463. The supercomputer resources for this study have been provided by the National High Performance Computing of Turkey (UHeM) under grant number 1008852020, supported by Associate Professor Zuhal Er, for which we are grateful. We are also thankful for the fruitful communications with Assistant Professor Garip Erdoğan and Şerzat Safaltın.

REFERENCES

(1) Reigada, D. C.; Prioli, R.; Jacobsohn, L. G.; Freire, F. L., Jr. Boron Carbide Films Deposited by a Magnetron Sputter−Ion Plating Process: Film Composition and Tribological Properties. *Diamond Relat. Mater.* **2000**, *9*, 489−493.

(2) Domnich, V.; Reynaud, S.; Haber, R. A.; Chhowalla, M. Boron Carbide: Structure, Properties, and Stability under Stress. *J. Am. Ceram. Soc.* **2011**, *94*, 3605−3628.

(3) Kuzenkova, M. A.; Kislyi, P. S.; Grabchuk, B. L.; Bodnaruk, N. I. The Structure and Properties of Sintered Boron Carbide. *J. Less Common Met.* **1979**, *67*, 217−223.

(4) Emin, D. Unusual Properties of Icosahedral Boron-Rich Solids. *J. Solid State Chem.* **2006**, *179*, 2791−2798.

(5) Thévenot, F. Boron Carbide—a Comprehensive Review. *J. Eur. Ceram. Soc.* **1990**, *6*, 205−225.

(6) Speyer, R. F.; Lee, H. Advances in Pressureless Densification of Boron Carbide. *J. Mater. Sci.* **2004**, *39*, 6017−6021.

(7) Lee, H.; Speyer, R. F.; Hackenberger, W. S. Sintering of Boron Carbide Heat-Treated with Hydrogen. *J. Am. Ceram. Soc.* **2002**, *85*, 2131−2133.

(8) Mashhadi, M.; Taheri-Nassaj, E.; Sglavo, V. M. Pressureless Sintering of Boron Carbide. *Ceram. Int.* **2010**, *36*, 151−159.

(9) Saeedi Heydari, M.; Baharvandi, H. R. Comparing the Effects of Different Sintering Methods for Ceramics on the Physical and Mechanical Properties of B4C−TiB2 Nanocomposites. *Int. J. Refract. Hard Met.* **2015**, *51*, 224−232.

(10) Kim, H.-W.; Koh, Y.-H.; Kim, H.-E. Densification and Mechanical Properties of B4C with Al2O3 as a Sintering Aid. *J. Am. Ceram. Soc.* **2000**, *83*, 2863−2865.

(11) Sun, J.; Liu, C.; Duan, C. Effect of Al and TiO2 on Sinterability and Mechanical Properties of Boron Carbide. *Mater. Sci. Eng.: A* **2009**, *509*, 89−93.

(12) Klotz, B. R.; Cho, K. C.; Dowding, R. J. Sintering Aids in the Consolidation of Boron Carbide (B4C) by the Plasma Pressure Compaction (P2C) Method. *Mater. Manuf. Process.* **2004**, *19*, 631−639.

(13) Skorokhod, V., Jr.; Vlajic, M. D.; Krstic, V. D. Mechanical Properties of Pressureless Sintered Boron Carbide Containing TiB2 Phase. *J. Mater. Sci. Lett.* **1996**, *15*, 1337−1339.

(14) Roy, T. K.; Subramanian, C.; Suri, A. K. Pressureless Sintering of Boron Carbide. *Ceram. Int.* **2006**, *32*, 227−233.

(15) Skorokhod, V.; Vlajić, M. D.; Krstić, V. D. Pressureless Sintering of B4C-TiB2 Ceramic Composites. *Mater. Sci. Forum* **1998**, *282-283*, 219−224.

(16) Baharvandi, H. R.; Hadian, A. M.; Alizadeh, A. Processing and Mechanical Properties of Boron Carbide−Titanium Diboride Ceramic Matrix Composites. *Appl. Compos. Mater.* **2006**, *13*, 191−198.

(17) da Rocha, R. M.; de Melo, F. C. L. Effect of TiO2 and TiB2 on Pressureless Sintering of B4C. *Mater. Sci. Forum* **2012**, *727-728*, 1022−1027.

(18) Skorokhod, V.; Processing, V. Microstructure, and Mechanical Properties of B4C — TiB2 Particulate Sintered Composites. Part I. Pressureless Sintering and Microstructure Evolution. *Powder Metall. Met. Ceram.* **2000**, *39*, 414−423.

(19) Skorokhod, V.; Processing, V. Microstructure, and Mechanical Properties of B4C — TiB2 Particulate Sintered Composites. Part II. Fracture and Mechanical Properties. *Powder Metall. Met. Ceram.* **2000**, *39*, 504−513.

(20) Liu, A. D.; Qiao, Y. J.; Liu, Y. Y. Pressureless Sintering and Properties of Boron Carbide-Titanium Diboride Composites by in Situ Reaction. *Key Eng. Mater.* **2012**, *525-526*, 321−324.
(21) McCuiston, R. C.; LaSalvia, J. C.; Moser, B.Effect of Carbon Additions and B4C Particle Size on the Microstructure and Properties of B4C - TiB2 Composites. *Mechanical Properties and Performance of Engineering Ceramics and Composites III*2007, 257−268.
(22) Çakır, E.; Ergun, C.; Şahin, F. Ç.; Erden, İ. In Situ Synthesis of B4C / TiB2 Composites from Low Cost Sugar Based Precursor. *Defect Diffus. Forum* **2010**, *297-301*, 52−56.
(23) Yue, X. Y.; Zhao, S. M.; Yu, L.; Ru, H. Q. Microstructures and Mechanical Properties of B4C-TiB2 Composite Prepared by Hot Pressure Sintering. *Key Eng. Mater.* **2010**, *434-435*, 50−53.
(24) Skorokhod, V., Jr.; Krstic, V. D. High Strength-High Toughness B4C-TiB2 Composites. *J. Mater. Sci. Lett.* **2000**, *19*, 237−239.
(25) Yamada, S.; Hirao, K.; Yamauchi, Y.; Kanzaki, S. High Strength B4C−TiB2 Composites Fabricated by Reaction Hot-Pressing. *J. Eur. Ceram. Soc.* **2003**, *23*, 1123−1130.
(26) Tkachenko, Y. G.; Britun, V. F.; Bovkun, G. O.; Yurchenko, D. Z. Electroerosion Behavior of a Ceramic Based on Boron Carbide: Phase Composition, Structure, and Properties of Protective Spark Coatings. *Powder Metall. Met. Ceram.* **2005**, *44*, 537−544.
(27) Wang, G. F.; Zhang, J. H.; Zhang, C.; Zhang, K. F. Densification and Mechanical Properties of B4C Based Composites Sintered by Reaction Hot-Pressing. *Key Eng. Mater.* **2010**, *434-435*, 24−27.
(28) Sigl, L. S.; Kleebe, H.-J. Microcracking in B4C-TiB2 Composites. *J. Am. Ceram. Soc.* **1995**, *78*, 2374−2380.
(29) Bogomol, I.; Nishimura, T.; Vasylkiv, O.; Sakka, Y.; Loboda, P. Microstructure and High-Temperature Strength of B4C−TiB2 Composite Prepared by a Crucibleless Zone Melting Method. *J. Alloys Compd.* **2009**, *485*, 677−681.
(30) Huang, S. G.; Vanmeensel, K.; Van der Biest, O.; Vleugels, J. In Situ Synthesis and Densification of Submicrometer-Grained B4C−TiB2 Composites by Pulsed Electric Current Sintering. *J. Eur. Ceram. Soc.* **2011**, *31*, 637−644.
(31) Uygun, B.; Göller, G.; Onüralp, Y.; Şahin, F. Ç. Production and Characterization of Boron Carbide − Titanium Diboride Ceramics by Spark Plasma Sintering Method. *Adv. Sci. Technol.* **2010**, *63*, 68−73.
(32) Huang, S. G.; Vanmeensel, K.; Malek, O. J. A.; Van der Biest, O.; Vleugels, J. Microstructure and Mechanical Properties of Pulsed Electric Current Sintered B4C−TiB2 Composites. *Mater. Sci. Eng.: A* **2011**, *528*, 1302−1309.
(33) Xu, C.; Cai, Y.; Flodström, K.; Li, Z.; Esmaeilzadeh, S.; Zhang, G.-J. Spark Plasma Sintering of B4C Ceramics: The Effects of Milling Medium and tib2 Addition. *Int. J. Refract. Hard Met.* **2012**, *30*, 139−144.
(34) Nikzad, L.; Licheri, R.; Ebadzadeh, T.; Orrù, R.; Cao, G. Effect of Ball Milling on Reactive Spark Plasma Sintering of B4C−tib2 Composites. *Ceram. Int.* **2012**, *38*, 6469−6480.
(35) Nikzad, L.; Orrù, R.; Licheri, R.; Cao, G. Fabrication and Formation Mechanism of B4C-TiB2 Composite by Reactive Spark Plasma Sintering Using Unmilled and Mechanically Activated Reactants. *J. Am. Ceram. Soc.* **2012**, *95*, 3463−3471.
(36) Hulbert, D. M.; Jiang, D.; Dudina, D. V.; Mukherjee, A. K. The Synthesis and Consolidation of Hard Materials by Spark Plasma Sintering. *Int. J. Refract. Met. Hard Mater.* **2009**, *27*, 367−375.
(37) Dudina, D. V.; Hulbert, D. M.; Jiang, D.; Unuvar, C.; Cytron, S. J.; Mukherjee, A. K. In Situ Boron Carbide−Titanium Diboride Composites Prepared by Mechanical Milling and Subsequent Spark Plasma Sintering. *J. Mater. Sci.* **2008**, *43*, 3569−3576.
(38) Olevsky, E. A.; Froyen, L. Impact of Thermal Diffusion on Densification during SPS. *J. Am. Ceram. Soc.* **2009**, *92*, S122.
(39) Orrù, R.; Licheri, R.; Locci, A. M.; Cincotti, A.; Cao, G. Consolidation/Synthesis of Materials by Electric Current Activated/Assisted Sintering. *Mater. Sci. Eng.: R: Rep.* **2009**, *63*, 127−287.
(40) Munir, Z. A.; Anselmi-Tamburini, U.; Ohyanagi, M. The Effect of Electric Field and Pressure on the Synthesis and Consolidation of Materials: A Review of the Spark Plasma Sintering Method. *J. Mater. Sci.* **2006**, *41*, 763−777.
(41) Trapp, J.; Kieback, B. Fundamental Principles of Spark Plasma Sintering of Metals: Part I − Joule Heating Controlled by the Evolution of Powder Resistivity and Local Current Densities. *Powder Metall.* **2019**, *62*, 297−306.
(42) Khor, K. A.; Yu, L.-G.; Chan, S. H.; Chen, X. J. Densification of Plasma Sprayed YSZ Electrolytes by Spark Plasma Sintering (SPS). *J. Eur. Ceram. Soc.* **2003**, *23*, 1855−1863.
(43) Trapp, J.; Semenov, A.; Eberhardt, O.; Nöthe, M.; Wallmersperger, T.; Kieback, B. Fundamental Principles of Spark Plasma Sintering of Metals: Part II − about the Existence or Non-Existence of the 'Spark Plasma Effect'. *Powder Metall.* **2020**, *63*, 312−328.
(44) Zavaliangos, A.; Zhang, J.; Krammer, M.; Groza, J. R. Temperature Evolution during Field Activated Sintering. *Mater. Sci. Eng.: A* **2004**, *379*, 218−228.
(45) Yucheng, W.; Zhengyi, F. Study of Temperature Field in Spark Plasma Sintering. *Mater. Sci. Eng. B* **2002**, *90*, 34−37.
(46) Vorotilo, S.; Potanin, A. Y.; Iatsyuk, I. V.; Levashov, E. A. SHS of Silicon-Based Ceramics for the High-Temperature Applications. *Adv. Eng. Mater.* **2018**, *20*, No. 1800200.
(47) Rogachev, A. S.; Vadchenko, S. G.; Trusov, G. V.; Scheck, Y. B. Combined Use of SHS and SPS: Important Mechanistic Details. *Int. J. Self-Propag. High-Temp. Synth.* **2021**, *30*, 22−29.
(48) Moore, J. J.; Feng, H. J. Combustion Synthesis of Advanced Materials: Part I Reaction Parameters. *Prog. Mater. Sci.* **1995**, *39*, 243−273.
(49) Gusev, A. I. Phase Equilibria in the Ternary System Titanium−Boron−Carbon: The Sections TiCy−TiB2and B4Cy−TiB2. *J. Solid State Chem.* **1997**, *133*, 205−210.
(50) Duschanek, H.; Rogl, P.; Lukas, H. L. A Critical Assessment and Thermodynamic Calculation of the Boron-Carbon-Titanium (B-C-Ti) Ternary System. *J. Phase Equilib.* **1995**, *16*, 46−60.
(51) Ziemnicka-Sylwester, M. TiB2-Based Composites for Ultra-High-Temperature Devices, Fabricated by SHS, Combining Strong and Weak Exothermic Reactions. *Materials* **2013**, *6*, 1903−1919.
(52) Sakkaki, M.; Sadegh Moghanlou, F.; Vajdi, M.; Shahedi Asl, M.; Mohammadi, M.; Shokouhimehr, M. Numerical Simulation of Heat Transfer during Spark Plasma Sintering of Zirconium Diboride. *Ceram. Int.* **2020**, *46*, 4998−5007.
(53) Collet, R.; Le Gallet, S.; Charlot, F.; Lay, S.; Chaix, J.-M.; Bernard, F. Effect of Electric Current on SPS Densification of Spherical Copper Powder. *J. Manuf. Mater. Process.* **2021**, *5*, 119.
(54) Franz, R.; Wiedemann, G. Ueber Die Wärme-Leitungsfähigkeit Der Metalle. *Ann. Phys. Chem.* **1853**, *165*, 497−531.
(55) Mohammad Bagheri, S.; Vajdi, M.; Sadegh Moghanlou, F.; Sakkaki, M.; Mohammadi, M.; Shokouhimehr, M.; Shahedi Asl, M. Numerical Modeling of Heat Transfer during Spark Plasma Sintering of Titanium Carbide. *Ceram. Int.* **2020**, *46*, 7615−7624.
(56) Nili, B.; Subhash, G.; Tulenko, J. S. Coupled Electro-Thermo-Mechanical Simulation for Multiple Pellet Fabrication Using Spark Plasma Sintering. *J. Manuf. Sci. Eng.* **2018**, *140*, No. 051010.
(57) Bale, C. W.; Bélisle, E.; Chartrand, P.; Decterov, S. A.; Eriksson, G.; Gheribi, A. E.; Hack, K.; Jung, I. H.; Kang, Y. B.; Melançon, J.; et al. FactSage Thermochemical Software and Databases - 2010 - 2016. *Calphad* **2016**, *54*, 35−53. www.factsage.com
(58) Gunjishima, I.; Akashi, T.; Goto, T. Characterization of Directionally Solidified B4C-TiB2 Composites Prepared by a Floating Zone Method. *Mater. Trans.* **2002**, *43*, 712−720.
(59) Perdew, J. P.; Burke, K.; Ernzerhof, M. Generalized Gradient Approximation Made Simple. *Phys. Rev. Lett.* **1996**, *77*, 3865−3868.
(60) Blöchl, P. E. Projector Augmented-Wave Method. *Phys. Rev. B* **1994**, *50*, 17953−17979.
(61) Tuckerman, M. E.; Martyna, G. J. Understanding Modern Molecular Dynamics: Techniques and Applications. *J. Phys. Chem. B* **2000**, *104*, 159−178.
(62) Baras, F.; Turlo, V.; Politano, O.; Vadchenko, S. G.; Rogachev, A. S.; Mukasyan, A. S. SHS in Ni/Al Nanofoils: A Review of

https://doi.org/10.1021/acs.jpcc.2c06179
J. Phys. Chem. C XXXX, XXX, XXX−XXX

Experiments and Molecular Dynamics Simulations. *Adv. Eng. Mater.* **2018**, *20*, No. 1800091.
(63) Kresse, G.; Joubert, D. From Ultrasoft Pseudopotentials to the Projector Augmented-Wave Method. *Phys. Rev. B* **1999**, *59*, 1758−1775.
(64) *MedeA version 3.4.0*; MedeA is a registered trademark of Materials Design, Inc.: San Diego, USA.
(65) Chandler, D., *Introduction to modern statistical mechanics*; Oxford Univ. Press: New York, NY, 2009.
(66) Ni, D. R.; Geng, L.; Zhang, J.; Zheng, Z. Z. Effect of B4C Particle Size on Microstructure of in Situ Titanium Matrix Composites Prepared by Reactive Processing of Ti−B4C System. *Scr. Mater.* **2006**, *55*, 429−432.
(67) Nartu, M. S. K. K. Y.; Mantri, S. A.; Pantawane, M. V.; Ho, Y.-H.; McWilliams, B.; Cho, K.; Dahotre, N. B.; Banerjee, R. In Situ Reactions during Direct Laser Deposition of Ti-B4C Composites. *Scr. Mater.* **2020**, *183*, 28−32.
(68) Zhao, Y.; Yu, T.; Chen, L.; Chen, Y.; Guan, C.; Sun, J. Microstructure and Wear Resistance Behavior of Ti−C−B4C-Reinforced Composite Coating. *Ceram. Int.* **2020**, *46*, 25136−25148.
(69) Corbin, N. D.; Resetar, T. M.; McCauley, J. W. "SHS" Self-Sintering of Materials in the Titanium-Boron-Carbon System. *Innov. Mater. Process.* **1985**, 337−346.
(70) Liu, Y.; Li, Z.; Peng, Y.; Huang, Y.; Huang, Z.; Zhang, D. Effect of Sintering Temperature and TIB2 Content on the Grain Size of B4C-tib2 Composites. *Mater. Today Commun.* **2020**, *23*, No. 100875.
(71) Olevsky, E. A.; Garcia-Cardona, C.; Bradbury, W. L.; Haines, C. D.; Martin, D. G.; Kapoor, D. Fundamental Aspects of Spark Plasma Sintering: II. Finite Element Analysis of Scalability. *J. Am. Ceram. Soc.* **2012**, *95*, 2414−2422.
(72) Hayun, S.; Kalabukhov, S.; Ezersky, V.; Dariel, M. P.; Frage, N. Microstructural Characterization of Spark Plasma Sintered Boron Carbide Ceramics. *Ceram. Int.* **2010**, *36*, 451−457.
(73) Anselmi-Tamburini, U.; Garay, J. E.; Munir, Z. A. Fundamental Investigations on the Spark Plasma Sintering/Synthesis Process. *Mater. Sci. Eng.: A* **2005**, *407*, 24−30.
(74) Huang, Z.; Wu, L.; Huang, Z.; Wu, L.Ultrahigh-Temperature Ceramics (UHTCS) Systems. *Phase Equilibria Diagrams of High Temperature Non-oxide Ceramics*; Springer2018, 103 −162.
(75) Mukasyan, A. S.; Shuck, C. E. Kinetics of SHS Reactions: A Review. *Int. J. Self-Propag. High-Temp. Synth.* **2017**, *26*, 145−165.

https://doi.org/10.1021/acs.jpcc.2c06179
J. Phys. Chem. C XXXX, XXX, XXX−XXX